Isolation of a Ru(IV) side-on peroxo intermediate in the water oxidation reaction

Casadevall, Carla; Martin-Diaconescu, Vlad; Browne, Wesley R.; Fernandez, Sergio; Franco, Federico; Cabello, Noemi; Benet-Buchholz, Jordi; Lassalle-Kaiser, Benedikt; Lloret-Fillol, Julio

Published in:
Nature Chemistry

DOI:
10.1038/s41557-021-00702-5

Publication date:
2021

ARTICLES
https://doi.org/10.1038/s41557-021-00702-5

nature chemistry

Isolation of a Ru(IV) side-on peroxo intermediate in the water oxidation reaction

Carla Casadevall[1], Vlad Martin-Diaconescu[1], Wesley R. Browne[2], Sergio Fernández[1], Federico Franco[1], Noemí Cabello[1], Jordi Benet-Buchholz[1], Benedikt Lassalle-Kaiser[3] and Julio Lloret-Fillol[1,4] ✉

The electrons that nature uses to reduce CO_2 during photosynthesis come from water oxidation at the oxygen-evolving complex of photosystem II. Molecular catalysts have served as models to understand its mechanism, in particular the O–O bond-forming reaction, which is still not fully understood. Here we report a Ru(IV) side-on peroxo complex that serves as a 'missing link' for the species that form after the rate-determining O–O bond-forming step. The Ru(IV) side-on peroxo complex (η^2-1^{IV}–OO) is generated from the isolated Ru(IV) oxo complex (1^{IV}=O) in the presence of an excess of oxidant. The oxidation (IV) and spin state (singlet) of η^2-1^{IV}–OO were determined by a combination of experimental and theoretical studies. ^{18}O- and ^{2}H-labelling studies evidence the direct evolution of O_2 through the nucleophilic attack of a H_2O molecule on the highly electrophilic metal–oxo species via the formation of η^2-1^{IV}–OO. These studies demonstrate water nucleophilic attack as a viable mechanism for O–O bond formation, as previously proposed based on indirect evidence.

Water oxidation (WO) to dioxygen is pivotal in natural photosynthesis[1,2], and inspires the development of sustainable technologies for the synthesis of renewable fuels and chemicals[3,4]. Since the first WO complex (the 'blue dimer'[5]), the focus of molecular catalysts has centred on catalyst design and the characterization of the mechanisms and intermediates that govern the WO reaction[6–8]. In general, the formal mechanisms considered are the coupling between two radical M–O• (or M–oxyl) species and the acid–base mechanism in which a molecule of water attacks an electrophilic metal oxo species (Fig. 1)[1,6,9–12]. In both cases, the formation of the O–O bond is usually the step that determines the rate of the reaction, and therefore to facilitate the O–O bond formation should translate into better efficiencies. However, despite indirect proofs for both mechanisms, the evidence for a direct formation of the O–O bond from a M=O moiety is circumstantial[2,6,11–14]. In part, the challenge is to characterize the intermediates after the O–O bond-forming step, especially when this is the rate-determining step (RDS) of the reaction, which is usually the case. The formation of putative metal–peroxo complexes during catalysis has been a topic of debate over the past decades and remains so[15–24].

Since the first report of spectroscopically proposed η^2-Ru(IV)–O_2 species, [Ru(^{Me}bimpy)(bpy)(η^2-O_2)]$^{2+}$ (bimpy, bis(imino)pyridine; bpy, 2,2′-bipyridine), based on a Raman band at 1,015 cm^{-1} (ref. [16]), several structures have been proposed[13,18,25–27]. Recently, Garand and co-workers proposed the gas phase generation of ^{1}[Ru(tpy)(bpy)(η^2-O_2)]$^{2+}$ (tpy, 2,2′;6′,2″-terpyridine) by reacting O_2 with [Ru(tpy)(bpy)]$^{2+}$ (υ(O–O) = 1,150 cm^{-1} and 1,085 cm^{-1} with $^{18}O_2$)[18]. Yet, compelling evidence for the formation of M–peroxo species formed under catalytic conditions after the O–O bond formation has not been reported.

Here, we report the isolation and characterization of an elusive Ru(IV) side-on peroxo intermediate η^2-[Ru^{IV}(OO)(L)](PF$_6$)$_2$ (η^2-1^{IV}–OO, L = Py_2^{Me}tacn (tacn, 1,4,7-triazacyclononane) obtained via O–O bond formation from M=O under conditions relevant for catalytic WO with a previously reported [Ru^{II}(OH_2)(L)](PF$_6$)$_2$ (**1**) complex[27]. The η^2-1^{IV}–OO intermediate was previously postulated to be formed after the O–O bond-formation RDS by computational studies[27]. Kinetic studies showed a first-order reaction rate versus complex **1** and Ce^{IV} and ^{18}O-labelling experiments further proved that the O–O bond formation occurs via water nucleophilic attack (WNA)[27].

Results and discussion

Synthesis and characterization of η^2-1^{IV}–OO. The closed-shell η^2-1^{IV}–OO was prepared from **1**, [Ru^{III}(OH)(L)](PF$_6$)$_2$ (1^{III}–OH) or [Ru^{IV}(O)(L)](PF$_6$)$_2$ (1^{IV}=O) by varying the number of equivalents of added oxidant ($NaIO_4$, Fig. 2a and Supplementary Section 2). η^2-1^{IV}–OO was isolated by the reaction of 1^{IV}=O with 3 equiv. $NaIO_4$ in D_2O at room temperature (r.t.) for three hours, followed by saturation of the solution with ammonium hexafluorophosphate (NH_4PF_6) to give needle-shaped crystals after two days at 5 °C. Two different crystals were analysed to confirm unambiguously the structure, which showed an asymmetric unit that contains one molecule of the metal complex and two counterions (Fig. 2b and Supplementary Section 3). The X-ray crystal structures of η^2-1^{IV}–OO unequivocally revealed a mononuclear side-on peroxo coordination and, thus, the heptacoordinate configuration of the Ru centre. The complex displays a distorted pentagonal bipyramid geometry, which arises from the coordination of the peroxo moiety. The X-ray crystal data refinement clearly shows two oxygen atoms coordinated to the Ru centre with an occupancy of 1.0 for each oxygen atom.

The O–O distances in the isolated crystals were 1.353(10) and 1.367(9) Å and are consistent with the peroxo character of the O–O coordinated moiety, as supported by Raman, X-ray absorption spectroscopy (XAS) and density functional theory (DFT) modelling at the ωB97XD/6-31G(d)/SDD//ωB97XD/cc-pVTZ/

[1]Institute of Chemical Research of Catalonia (ICIQ), The Barcelona Institute of Science and Technology, Tarragona, Spain. [2]Molecular Inorganic Chemistry, Stratingh Institute for Chemistry, Faculty of Science and Engineering, University of Groningen, Groningen, the Netherlands. [3]Synchrotron SOLEIL, Gif-sur-Yvette, France. [4]Catalan Institution for Research and Advanced Studies (ICREA), Barcelona, Spain. ✉e-mail: jlloret@iciq.es

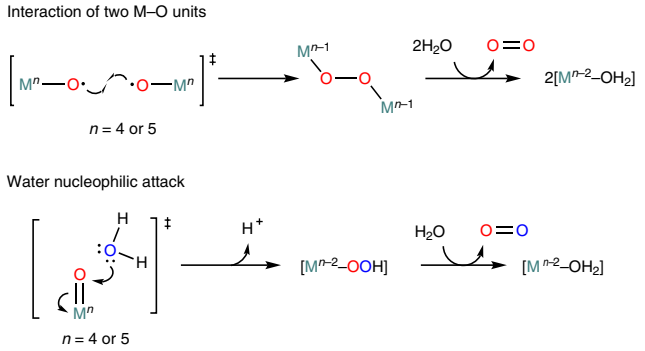

Fig. 1 | O–O bond-forming mechanisms. Formal mechanisms considered in the O–O bond formation.

SDD (Ru) level of theory (DFT-calculated O–O distance, $d_{(O-O)teor}$ = 1.359 Å for a singlet **η²-1^{IV}–OO** complex; Fig. 2)[21]. The O–O moiety is bound symmetrically to Ru with Ru–O distances and O1–Ru–O2 angle values that fall within those reported for Ru–O_2 complexes (d(O–O) = 1.36–1.46 Å, d(Ru–O) = 1.958–2.040 Å and α(O–Ru–O) = 39.7°) (ref. [28]). The analysis of the diffracted crystal by coldspray high-resolution mass spectrometry (CSI-HRMS) shows a prominent peak at m/z 604.0885 and an isotopic pattern that matches [**[η²-1^{IV}–OO]$^{2+}$+(PF$_6$)$^-$]$^+$** (Supplementary Fig. 35).

DFT calculations were used to estimate the relative stability of **η²-1^{IV}–OO** with respect to other isomers. Since previous studies have shown it difficult to accurately describe the O_2-binding modes in Ru–O_2 (ref. [17]), we used two different density functionals to model the possible isomers and compared them with experimental X-ray data. Both functionals, unrestricted ωB97XD and M11, agree that the closed-shell **^{1}[η²-1^{IV}–OO]** is the most stable isomer[17].

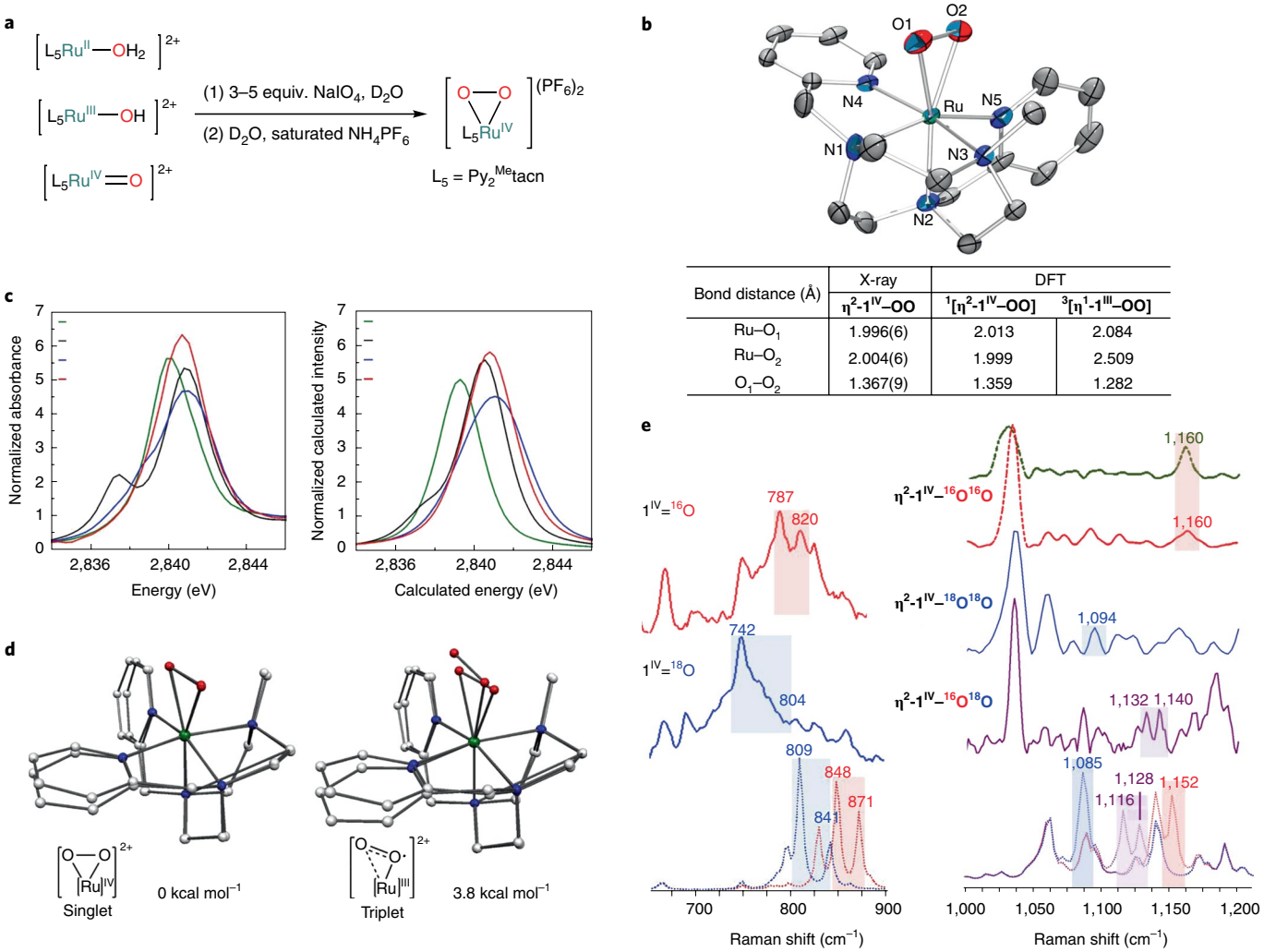

Bond distance (Å)	X-ray	DFT	
	η²-1^{IV}–OO	**^{1}[η²-1^{IV}–OO]**	**^{3}[η^1-1^{III}–OO]**
Ru–O_1	1.996(6)	2.013	2.084
Ru–O_2	2.004(6)	1.999	2.509
O_1–O_2	1.367(9)	1.359	1.282

Fig. 2 | Summary of the synthesis and spectroscopic characterization of a closed-shell Ru(IV) side-on peroxo intermediate (η²-1^{IV}–OO). a, **η²-1^{IV}–OO** was formed from the isolated **1**, **1^{III}–OH** and **1^{IV}=O** intermediates, using equivalent synthetic conditions. **b**, ORTEP drawing (thermal ellipsoids are drawn at a 50% probability level) of [Ru^{IV}(OO)(Py$_2$^{Me}tacn)](PF$_6$)$_{1.5}$(IO$_3$)$_{0.5}$ (**η²-1^{IV}–OO**). PF_6 anions and hydrogen atoms are omitted for clarity. ORTEP ellipsoids and DFT structures colour code: Ru, green; O, red; C, grey; N, blue. The X-ray and DFT bond distances in the table illustrate a better agreement with the Ru(IV) side-on geometry and singlet electronic structure. **c**, Comparison between the experimental (left) and theoretical (right) Ru L_3-edge XAS of **1** (green line), **1^{III}–OH** (black line), **1^{IV}=O** (blue line) and **η²-1^{IV}–OO** (red line). **d**, The overlap X-ray and DFT-optimized structures of **η²-1^{IV}–OO** in the singlet and the triplet spin states. **e**, Left: solid-state Raman spectra of the isolated **1^{IV}=O** (λ_{exc} = 632.8 nm, 600 μW power at r.t.) with ^{16}O (red spectrum) and ^{18}O (blue spectrum) isotopic substitution. Right: solution Raman spectra of the in situ generated **η²-1^{IV}–OO** (λ_{exc} = 457 nm, 50 mW power at r.t.) from **1^{IV}=O** in MilliQ H_2O (green and red spectra generated with cerium(IV) ammonium nitrate (CAN) and $NaIO_4$, respectively, as the sacrificial oxidants) and from **1^{IV}=^{18}O** in $H_2{}^{18}O$ with $NaIO_4$ (blue spectrum) and D_2O (purple spectrum) (2 mM), in the region of the O–O stretch.

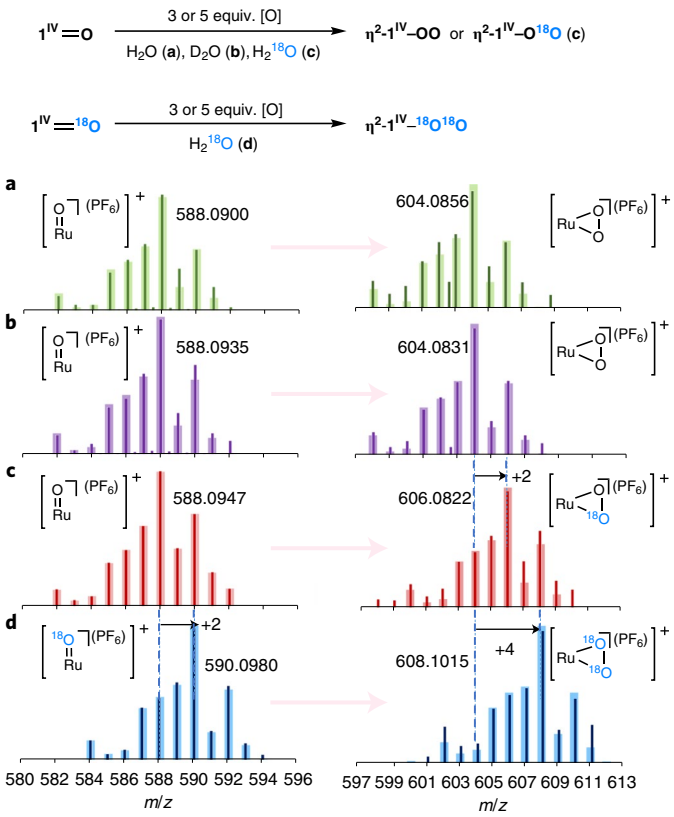

Fig. 3 | CSI-HRMS isotopic labelling experiments evidencing the WNA mechanism. a,**b**, CSI-HRMS (293 K) of the monocharged $[Ru\text{-}OO\text{-}(PF_6)]^+$ species of **η²-1ᴵⱽ–OO** generated after the addition of $NaIO_4$ (3 equiv.) to the isolated **1ᴵⱽ=O** in MilliQ H_2O (**a**) and in D_2O (**b**). **c**, CSI-HRMS (293 K) of the monocharged $[Ru\text{-}O^{18}O\text{-}(PF_6)]^+$ species of **η²-1ᴵⱽ–O¹⁸O** generated after the addition of $NaIO_4$ (3 equiv.) to the isolated **1ᴵⱽ=O** in $H_2{}^{18}O$. **d**, CSI-HRMS (293 K) of the monocharged $[Ru\text{-}O^{18}O\text{-}(PF_6)]^+$ species of **η²-1ᴵⱽ–¹⁸O¹⁸O** generated in $H_2{}^{18}O$ after the addition of $NaIO_4$ (3 equiv.) to the isolated **1ᴵⱽ=¹⁸O**. The experimental data (bars) are directly compared with the simulated isotopic pattern (shaded region). Black arrows in the spectra and dashed blue lines indicate the *m*/*z* shift on ^{18}O labelling. The observed shift of *m*/*z* +2 in $H_2{}^{18}O$ agrees with the incorporation of one ^{18}O into the peroxo moiety in the formed **η²-1ᴵⱽ–O¹⁸O** intermediate when starting with **1ᴵⱽ=O** after the WNA. The observed shift of *m*/*z* +4 in $H_2{}^{18}O$ with respect to that of **η²-1ᴵⱽ–OO** agrees with the two oxygens of the peroxo group being ^{18}O in the final **η²-1ᴵⱽ–¹⁸O¹⁸O** intermediate when starting with **1ᴵⱽ=¹⁸O** after the WNA.

¹[η²-1ᴵⱽ–OO] is 3.8 kcal mol^{-1} lower in energy than **³[η¹-1ᴵᴵᴵ–OO]** at the ωB97XD/6-31G(d)/SDD//ωB97XD/cc-pVTZ/SDD (Ru) level of theory. The calculated geometry of **¹[η²-1ᴵⱽ–OO]** overlaps better with the X-ray structure (Fig. 2d and Supplementary Tables 7 and 8). This agrees with the silent electron spin resonance spectrum obtained (Supplementary Fig. 8).

The electronic structure of **η²-1ᴵⱽ–OO** was probed by Ru L_3-edge XAS (Fig. 2c) and **1**, **1ᴵᴵᴵ–OH** and **1ᴵⱽ=O** were measured as references. **η²-1ᴵⱽ–OO** shows a single intense feature at 2,838.0 eV, consistent with a closely spaced *d* manifold in a heptacoordinate metal centre. Furthermore, the electronic structure of the **η²-1ᴵⱽ–OO** bond alludes to a peroxo moiety (Supplementary Section 5)[29].

The Raman spectrum of **η²-1ᴵⱽ–OO** in water shows a band at 1,160 cm^{-1} that exhibits an isotope shift of 66 cm^{-1} on ^{18}O-substitution (1,094 cm^{-1}, $\Delta^{16,18}{}_{(DFT\text{-}calcd)} = 67$ cm^{-1}), which was assigned to the O–O stretch (Fig. 2e and Supplementary Section 6). This frequency is within the range of the O–O stretch of related M–O_2 complexes[16,18–20]. The observed O–O stretch agrees with the formation of a closed-shell heptacoordinate **η²-1ᴵⱽ–OO** intermediate, as supported by the DFT-calculated Raman spectra. The calculated O–O stretch of **¹[η²-1ᴵⱽ–OO]**, appears at 1,152 cm^{-1}, whereas an O–O stretch for **³[η¹-1ᴵᴵᴵ–OO]** is observed at 1,297 cm^{-1} (Supplementary Figs. 26–28)[16–18,25]. In contrast, the Raman spectrum of **1ᴵⱽ=O** shows a Fermi doublet at 787 and 820 cm^{-1} that exhibits an isotope shift of 45 and 50 cm^{-1}, respectively, on ^{18}O substitution, and so was assigned to the Ru–O stretch (Fig. 2e and Supplementary Figs. 22–25).

Study of the O–O bond formation by isotopic labelling. The in situ formation of **η²-1ᴵⱽ–OO** from the isolated **1ᴵⱽ=O** was investigated by solution Raman and CSI-HRMS labelling studies in MilliQ H_2O, D_2O and $H_2{}^{18}O$ (Supplementary Sections 6 and 7). As the oxo group of **1ⁱᵛ=O** does not exchange in $H_2{}^{18}O$ to form **1ᴵⱽ=¹⁸O** within the experimental time and set-up conditions[27], ^{18}O-labelling experiments can be used to track the O–O bond formation event by analysing the nature of the resulting **η²-1ᴵⱽ–OO**. Solution Raman measurements of the in situ generated **η²-1ᴵⱽ–OO** intermediate from the oxidation of **1ᴵⱽ=O** by $NaIO_4$ and Ce^{IV} in MilliQ H_2O, D_2O or $H_2{}^{18}O$ agreed with the formation of a side-on coordinated **η²-1ᴵⱽ–OO** intermediate. A redshift and a split of the O–O stretch band associated with the side-on **η²-1ᴵⱽ–OO** intermediate was observed due to the incorporation of one ^{18}O into the final **η²-1ᴵⱽ–O¹⁸O** (two bands at −28 and −20 cm^{-1} with respect to the single band observed in **η²-1ᴵⱽ–OO**) or **η²-1ᴵⱽ–¹⁸O¹⁸O** (−66 cm^{-1}) when it was generated from the isolated **1ᴵⱽ=O** or **1ᴵⱽ=¹⁸O** in $H_2{}^{18}O$, respectively (Fig. 2e and Supplementary Figs. 26–32). Likewise, CSI-HRMS monitoring of a solution that contained **1ᴵⱽ=O** (2 mM) and $NaIO_4$ (5 equiv.) in MilliQ H_2O (or D_2O) showed the formation of a prominent peak at *m*/*z* 634.0100 and a less intense one at *m*/*z* 604.0885, isotopic patterns associated with **[[η²-1ᴵⱽ–OO]²⁺+(IO₃)⁻]⁺** and **[[η²-1ᴵⱽ–OO]²⁺+(PF₆)⁻]⁺**, respectively (Fig. 3 and Supplementary Figs. 50–53), which rule out any H/D exchange during the process. The intensity of the **[[η²-1ᴵⱽ–OO]²⁺+(PF₆)⁻]⁺** peak increases over time due to the accumulation of the intermediate until it reached a plateau (about six hours) due to the formation of **[η²-1ᴵⱽ–OO]²⁺** crystals, as observed by microscopy and Raman spectroscopy (Supplementary Fig. 48). This suggests that **η²-1ᴵⱽ–OO** could be isolated under cold-saturated conditions due to its insolubility (Supplementary Table 10). In addition, a new peak at *m*/*z* 229.5601, which corresponds to the dicharged **[η²-1ᴵⱽ–OO]²⁺** complex, appeared during the reaction time. These peaks upshifted by *m*/*z* 8, 2 and 1 with $H_2{}^{18}O$ as the solvent (*m*/*z* 642.0313, 606.0944 and 230.5649, respectively), and were assigned to the mix-labelled Ru(IV)–peroxo species **[[η²-1ᴵⱽ–O¹⁸O]²⁺+(I¹⁸O₃)⁻]⁺**, **[[η²-1ᴵⱽ–O¹⁸O]²⁺+(PF₆)⁻]⁺** and **[η²-1ᴵⱽ–O¹⁸O]²⁺**, respectively (Fig. 3 and Supplementary Sections 7.3 and 7.4). The same peaks were obtained when starting with **1ᴵⱽ=¹⁸O** (2 mM), after treatment with $NaIO_4$ (3 equiv.) in $H_2{}^{16}O$. When the reaction was performed from **1ᴵⱽ=¹⁸O** in $H_2{}^{18}O$ these peaks upshifted by *m*/*z* of 10, 4 and 2, respectively, regarding the unlabelled compounds, associated with **[η²-1ᴵⱽ–¹⁸O¹⁸O]²⁺**, **[[η²-1ᴵⱽ–¹⁸O¹⁸O]²⁺+(PF₆)⁻]⁺** and **[[η²-1ᴵⱽ–¹⁸O¹⁸O]²⁺+(I¹⁸O₃)⁻]⁺**, respectively (Supplementary Figs. 44–47). Control experiments showed no O–O exchange of the coordinated peroxo moiety on the addition of H_2O to a solution of **η²-1ᴵⱽ–O¹⁸O** in $H_2{}^{18}O$ (Supplementary Fig. 56). Moreover, the fact that we obtained analogous results with the single electron transfer Ce^{IV} ($Ce(OTf)_4$) supports the formation on this in-cycle **η²-1ᴵⱽ–OO** intermediate via WNA (Supplementary Fig. 57).

Mechanistic studies. At this point, a key aspect is to further understand the connection between the isolated **1ᴵⱽ=O** and **η²-1ᴵⱽ–OO**, as well as its role in the catalytic cycle. First, electrochemical and ultraviolet–visible spectroelectrochemical studies on the isolated **1ᴵⱽ=O** intermediate show an irreversible oxidation at 1.85 V versus the normal hydrogen electrode (NHE) (1.77 V versus NHE

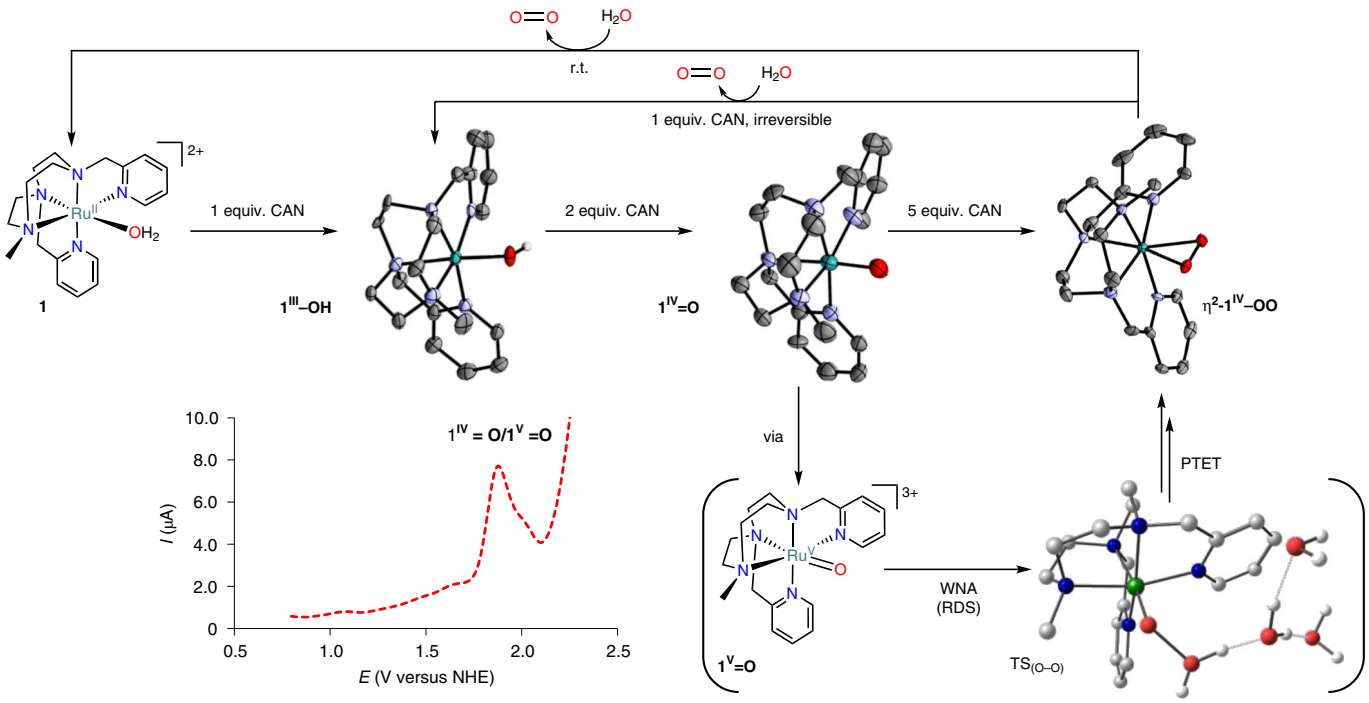

Fig. 4 | Summary of the reactivity of the Ru intermediates in relation to the WO catalytic cycle. Formation and reactivity of ruthenium intermediates involved in WO catalysed by complex **1**. Inset: square wave voltammogram (SWV) of $\mathbf{1^{IV}{=}O}$ (1 mM) in a $TBAPF_6$ (0.1 M) propylene carbonate solution under an Ar atmosphere. All the isolated intermediates were catalytically competent with equivalent turnover number and turnover frequency values. The mixed compound labelled $\mathbf{\eta^2\text{-}1^{IV}\text{–}{}^{16}O^{18}O}$ unequivocally confirmed its generation after WNA onto the highly electrophilic $\mathbf{1^{V}{=}O}$ species. Likewise, dioxygen $\mathbf{{}^{16}O{=}{}^{18}O}$ evolved when starting with the $\mathbf{\eta^2\text{-}1^{IV}\text{–}{}^{16}O^{18}O}$ intermediate, which confirms the direct oxygen evolution from the isolated Ru(IV) side-on peroxo intermediate. The colour code for the ORTEP ellipsoids and DFT structures: Ru, green; O, red; C, grey; H, white; N, blue. PTET, proton transfer electron transfer. TS, transition state.

obtained by DFT calculations; Supplementary Section 10), which can be assigned to the $\mathbf{1^{IV/V}}$ oxo couple (Fig. 4. and Supplementary Section 8). Previously, $\mathbf{1^{V}{=}O}$ has been suggested as the active species responsible for the O–O bond formation event on the basis of kinetic and computational studies[27].

Computational studies to model the full catalytic cycle at the ωB97XD/6-31G(d)/SDD (Ru)//ωB97XD/cc-pVTZ/SDD (Ru) level of theory located the O–O bond formation after the redox pre-equilibrium of the $\mathbf{1^{IV}{=}O}$ to $\mathbf{1^{V}{=}O}$ oxidation (Supplementary Section 10). This is in agreement with our previously observed redox dependence of the WO reaction catalysed by complex **1** on the basis of kinetic studies[27]. Indeed, all the redox processes are exergonic in the presence of an excess of Ce^{IV} (catalytic conditions), except for the oxidation of $\mathbf{1^{IV}{=}O}$ to $\mathbf{1^{V}{=}O}$. Then, the activation energy obtained from the Eyring equation is consistent with that obtained for the WNA O–O bond formation by DFT (26 ± 2 versus 23 kcal mol^{-1}, respectively; see Supplementary Sections 9.3 and 10 for details). Both theory and experiment suggest that the O–O bond formation is the RDS of the reaction, as judged by the negative $\Delta S^{\ddagger}$ value obtained from the Eyring plot (-29 ± 3 versus -32 cal mol^{-1}), in agreement with an associative mechanism[30].

Further evidence on the nature of the RDS is the rapid O_2 evolution (less than five seconds) after the addition of Ce^{IV} (1 equiv.) either to the mixed labelled $\mathbf{\eta^2\text{-}1^{IV}\text{–}{}^{18}O^{16}O}$ or to $\mathbf{\eta^2\text{-}1^{IV}\text{–}OO}$ in water to yield 1 equiv. $^{34}O_2$ or $^{32}O_2$, respectively, and Ru(III) species. Moreover, the O_2 release from $\mathbf{\eta^2\text{-}1^{IV}\text{–}OO}$ after the addition of 1 equiv. Ce^{IV} was more than 30-fold faster than that when starting from $\mathbf{1^{IV}{=}O}$ in the presence of a 100-fold excess of Ce^{IV} (Supplementary Fig. 67 and Supplementary Scheme 1) [23]. This evidence rules out the O_2 release from $\mathbf{\eta^2\text{-}1^{IV}\text{–}OO}$ as the RDS. Accordingly, DFT calculations show a barrierless O_2 release from the dioxygen-adduct $\mathbf{1^{III}\text{–}O_2}$ (Supplementary Figs. 83 and 84, and Supplementary Table 14). The calculated transition state for the O_2 release from $\mathbf{\eta^2\text{-}1^{IV}\text{–}OO}$ (>40 kcal mol^{-1}) supports its accumulation in solution at a low concentration of sacrificial oxidant (Supplementary Table 14). The spin conversion to release triplet O_2 could provide an explanation for the slow O_2 release in the absence of additional oxidation.

Catalytic tests for WO from isolated intermediates (**1**, $\mathbf{1^{III}\text{–}OH}$, $\mathbf{1^{IV}{=}O}$ and $\mathbf{\eta^2\text{-}1^{IV}\text{–}OO}$) showed similar initial O_2 turnover frequencies and numbers (Supplementary Table 11 and Supplementary Fig. 68), consistent with $\mathbf{\eta^2\text{-}1^{IV}\text{–}OO}$ being an intermediate of the catalytic cycle. Moreover, the decay of $\mathbf{\eta^2\text{-}1^{IV}\text{–}OO}$ crystals in acetonitrile gives a Ru(II) species (Fig. 4 and Supplementary Figs. 70 and 71). Additionally, attempts to obtain $\mathbf{\eta^2\text{-}1^{IV}\text{–}OO}$ under O_2 pressure (up to 20 bar) either in acetone or D_2O as solvents or using H_2O_2 in the presence of Et_3N did not yield the desired product, which rules out that the O_2 formed, or the potentially formed H_2O_2, during WO catalysis is responsible for the formation of $\mathbf{\eta^2\text{-}1^{IV}\text{–}OO}$ (Supplementary Fig. 72).

Lastly, a microkinetic model elaborated with the theoretical mechanism and fitted with experimental kinetic data shows that the accumulation of $\mathbf{\eta^2\text{-}1^{IV}\text{–}OO}$ is feasible under a low concentration of sacrificial oxidant (Supplementary Section 11). The kinetic model supports the isolation of $\mathbf{\eta^2\text{-}1^{IV}\text{–}OO}$ as a solid in the presence of ammonium hexafluorophosphate as the precipitating agent (Supplementary Figs. 88 and 89). This mathematical model indicates that an intermediate after the RDS can be trapped in a thermodynamic sink, such as a precipitation equilibrium. Altogether, this is compatible with a catalytic cycle in which $\mathbf{1^{IV}{=}O}$ is the resting state and $\mathbf{\eta^2\text{-}1^{IV}\text{–}OO}$ is transiently formed under catalytic conditions after the RDS. In contrast, by proper modification of the reaction conditions, the elusive $\mathbf{\eta^2\text{-}1^{IV}\text{–}OO}$ can be accumulated and isolated as a

solid material. Also, the direct tracking of the O–O bond formation by isotopic labelling from $\mathbf{1^{V}{=}O}$ to $\mathbf{\eta^2\text{-}1^{IV}{-}OO}$ supports the nucleophilic attack of water on $\mathbf{1^{V}{=}O}$ to form the O–O bond (RDS) (Fig. 4).

Conclusion

In conclusion, peroxo species have long been postulated as a key intermediate after the O–O bond formation via WNA. Nevertheless, it has only been transiently observed. Here we report a crystallized and isolated $\mathbf{\eta^2\text{-}[Ru^{IV}(OO)(Py_2^{Me}tacn)](PF_6)_2}$ complex generated under catalytic conditions from all the previous isolated intermediates of the catalytic cycle, which is formed after the O–O bond formation event. All the spectroscopic characterization is consistent with a side-on coordination of the peroxo moiety to a closed shell Ru(IV), which is in good agreement with our computational studies. Moreover, the mixed labelled $^{16}O^{18}O$ Ru(IV)–peroxo complex ($\mathbf{\eta^2\text{-}1^{IV}{-}O^{18}O}$) formed on the addition of an excess of Ce^{IV} (single electron oxidant) to $\mathbf{1^{IV}{=}^{16}O}$ (intermediate before the RDS) in $H_2{}^{18}O$ points to the formation of the O–O bond via a WNA mechanism. These results prove that the WO mechanism can operate with a single metal site; as one of the proposed mechanisms in an oxygen-evolving complex, in which the M=O species undergoes a nucleophilic attack by water to form the O–O bond in the coordination sphere of the metal site. The isolated $\mathbf{\eta^2\text{-}1^{IV}{-}OO}$ intermediate is one of the potential missing links after the RDS, but other missing species need to be revealed to have a more complete view of the post-RDS WO catalytic cycle. This discovery clarifies our understanding of the O–O bond formation event by a direct tracking of the species before and after the RDS.

Online content

Any methods, additional references, Nature Research reporting summaries, source data, extended data, supplementary information, acknowledgements, peer review information; details of author contributions and competing interests; and statements of data and code availability are available at https://doi.org/10.1038/s41557-021-00702-5.

Received: 13 September 2019; Accepted: 12 April 2021;
Published online: 31 May 2021

References

1. Cox, N., Pantazis, D. A., Neese, F. & Lubitz, W. Biological water oxidation. *Acc. Chem. Res.* **46**, 1588–1596 (2013).
2. Lubitz, W., Chrysina, M. & Cox, N. Water oxidation in photosystem II. *Photosynth. Res.* **142**, 105–125 (2019).
3. Field, C. B., Behrenfeld, M. J., Randerson, J. T. & Falkowski, P. Primary production of the biosphere: integrating terrestrial and oceanic components. *Science* **281**, 237–240 (1998).
4. Lewis, N. S. Research opportunities to advance solar energy utilization. *Science* **351**, aad1920 (2016).
5. Gersten, S. W., Samuels, G. J. & Meyer, T. J. Catalytic oxidation of water by an oxo-bridged ruthenium dimer. *J. Am. Chem. Soc.* **104**, 4029–4030 (1982).
6. Zhang, B. & Sun, L. Artificial photosynthesis: opportunities and challenges of molecular catalysts. *Chem. Soc. Rev.* **48**, 2216–2264 (2019).
7. Karkas, M. D., Verho, O., Johnston, E. V. & Akermark, B. Artificial photosynthesis: molecular systems for catalytic water oxidation. *Chem. Rev.* **114**, 11863–12001 (2014).
8. Sartorel, A. et al. Polyoxometalate embedding of a tetraruthenium(iv)-oxo-core by template-directed metalation of $[\gamma\text{-}SiW_{10}O_{36}]^{8-}$: a totally inorganic oxygen-evolving catalyst. *J. Am. Chem. Soc.* **130**, 5006–5007 (2008).
9. Pantazis, D. A. Missing pieces in the puzzle of biological water oxidation. *ACS Catal.* **8**, 9477–9507 (2018).
10. Blakemore, J. D., Crabtree, R. H. & Brudvig, G. W. Molecular catalysts for water oxidation. *Chem. Rev.* **115**, 12974–13005 (2015).
11. Lloret-Fillol, J. & Costas, M. in *Advances in Organometallic Chem*istry Vol. 71 (ed. Pérez, P. J.) 1–52 (Academic, 2019).
12. Fukuzumi, S., Lee, Y.-M. & Nam, W. Kinetics and mechanisms of catalytic water oxidation. *Dalton Trans.* **48**, 779–798 (2019).
13. Shaffer, D. W., Xie, Y. & Concepcion, J. J. O–O bond formation in ruthenium-catalyzed water oxidation: single-site nucleophilic attack vs. O–O radical coupling. *Chem. Soc. Rev.* **46**, 6170–6193 (2017).
14. Gamba, I., Codolà, Z., Lloret-Fillol, J. & Costas, M. Making and breaking of the OO bond at iron complexes. *Coord. Chem. Rev.* **334**, 2–24 (2017).
15. Wasylenko, D. J. et al. Electronic modification of the $[Ru^{II}(tpy)(bpy)(OH_2)]^{2+}$ scaffold: effects on catalytic water oxidation. *J. Am. Chem. Soc.* **132**, 16094–16106 (2010).
16. Concepcion, J. J., Tsai, M. K., Muckerman, J. T. & Meyer, T. J. Mechanism of water oxidation by single-site ruthenium complex catalysts. *J. Am. Chem. Soc.* **132**, 1545–1557 (2010).
17. Kang, R., Yao, J., Chen, H. & Are, D. F. T. Methods accurate in mononuclear ruthenium-catalyzed water oxidation? An ab initio assessment. *J. Chem. Theory Comput.* **9**, 1872–1879 (2013).
18. Duffy, E. M., Marsh, B. M., Voss, J. M. & Garand, E. Characterization of the oxygen binding motif in a ruthenium water oxidation catalyst by vibrational spectroscopy. *Angew. Chem. Int. Ed.* **55**, 4079–4082 (2016).
19. Cramer, C. J., Tolman, W. B., Theopold, K. H. & Rheingold, A. L. Variable character of O–O and M–O bonding in side-on (η^2) 1:1 metal complexes of O_2. *Proc. Natl. Acad. Sci. USA* **100**, 3635–3640 (2003).
20. Holland, P. L. Metal–dioxygen and metal–dinitrogen complexes: where are the electrons? *Dalton Trans.* **39**, 5415–5425 (2010).
21. Company, A., Lloret-Fillol, J. & Costas, M. in *Comprehensive Inorganic Chemistry II* 2nd edn (eds Reedijk, J. & Poeppelmeier, K) 487–564 (Elsevier, 2013).
22. Cho, J. et al. Structure and reactivity of a mononuclear non-haem iron(III)–peroxo complex. *Nature* **478**, 502–505 (2011).
23. Bang, S. et al. Redox-inactive metal ions modulate the reactivity and oxygen release of mononuclear non-haem iron(III)–peroxo complexes. *Nat. Chem.* **6**, 934–940 (2014).
24. Fukuzumi, S. et al. Catalytic four-electron reduction of O_2 via rate-determining proton-coupled electron transfer to a dinuclear cobalt-μ-1,2-peroxo complex. *J. Am. Chem. Soc.* **134**, 9906–9909 (2012).
25. Polyansky, D. E. et al. Water oxidation by a mononuclear ruthenium catalyst: characterization of the intermediates. *J. Am. Chem. Soc.* **133**, 14649–14665 (2011).
26. Wang, L., Wu, Q. & Voorhis, T. V. Acid–base mechanism for ruthenium water oxidation catalysts. *Inorg. Chem.* **49**, 4543–4553 (2010).
27. Casadevall, C., Codolà, Z., Costas, M. & Lloret-Fillol, J. Spectroscopic, electrochemical and computational characterisation of Ru species involved in catalytic water oxidation: evidence for a $[Ru^{V}(O)(Py_2^{Me}tacn)]$ intermediate. *Chem. Eur. J.* **22**, 10111–10126 (2016).
28. Shen, J., Stevens, E. D. & Nolan, S. P. Synthesis and reactivity of the ruthenium(II) dihydride $Ru(Ph_2PNMeNMePPh_2)_2H_2$. *Organometallics* **17**, 3875–3882 (1998).
29. Cho, J., Sarangi, R. & Nam, W. Mononuclear metal–O_2 complexes bearing macrocyclic *N*-tetramethylated cyclam ligands. *Acc. Chem. Res.* **45**, 1321–1330 (2012).
30. Savini, A. et al. Mechanistic aspects of water oxidation catalyzed by organometallic iridium complexes. *Eur. J. Inorg. Chem.* **2014**, 690–697 (2014).

Methods

$Py_2^{Me}tacn$ and complex **1** were synthesized according to previously reported procedures[27]. Isolated intermediates $\mathbf{1^{III}–OH}$ and $\mathbf{1^{IV}=O}$ were prepared starting from complex **1** with the addition of an oxidant ($NaIO_4$, 0.5 and 1.5 equiv., respectively) and further precipitation with an ammonium hexafluorophosphate saturated solution in degassed MilliQ water and then cooling to 5 °C. Likewise, intermediate $\mathbf{\eta^2\text{-}1^{IV}–OO}$ was isolated from all the previous intermediates on the addition of different equivalents of oxidant and further slow precipitation at 5 °C. See the Supplementary Information for further synthetic procedure details, physical methods and detailed procedures for the characterization techniques used.

Data availability

The crystallographic data for $\mathbf{\eta^2\text{-}[Ru^{IV}(OO)(Py_2^{Me}tacn)](PF_6)_{1.5}(IO_3)_{0.5}}$, $\mathbf{\eta^2\text{-}[Ru^{IV}(OO)(Py_2^{Me}tacn)](PF_6)_2}$ and $\mathbf{1^{IV}=O}$ have been deposited with the Cambridge Crystallographic Data Centre under accession numbers 1944703, 1944703 and 1944705, respectively. The data supporting the findings of the current study are available within the paper and its Supplementary Information.

Acknowledgements

We thank the ICIQ Foundation, MEC for PhD grants FPU14/02550 (C.C.) and FPU16/04234 (S.F.), and for the AP2Chem project (Ref: PID2019-110050RB-I00), the European Research Foundation for project FP7-PEOPLE-2010-ERG-268445 (J.L.-F.) and the CELLEX Foundation through the CELLEX-ICIQ high-throughput experimentation platform, the Netherlands Ministry of Education, Culture and Science (Gravity Program 024.001.035, W.R.B.) for financial support. We acknowledge Catexel for the generous gift of 1,4,7-tritosyl-1,4,7-triazacyclononane (Ts_3tacn).

We acknowledge the LUCIA Beamline staff at SOLEIL synchrotron where the XAS data was collected (V.M.-D.).

Author contributions

J.L.-F. and C.C. directed and conceived this project. C.C. synthesized all the intermediates, performed most of the experimental work, the DFT studies, the kinetic model and wrote the draft of the manuscript. V.M.-D., C.C., F.F. and B.L.-K. performed the synchrotron measurements and V.M.-D. analysed the data. W.R.B. and C.C. performed the Raman measurements and the analyses. V.M.-D. and C.C. performed the electron spin resonance experiments. S.F. performed the studies to calculate the activation parameters. C.C. and F.F. performed the electrochemical studies. N.C. optimized the experimental parameters of CSI-HRMS and, together with C.C., performed the CSI-HRMS studies and analysed the data. J.B.-B. performed the crystallographic analyses of the isolated intermediates. All the authors discussed the results and contributed to the manuscript.

Competing interests

The authors declare no competing interests.

Additional information

Supplementary information The online version contains supplementary material available at https://doi.org/10.1038/s41557-021-00702-5.

Correspondence and requests for materials should be addressed to J.L.-F.

Peer review information *Nature Chemistry* thanks the anonymous reviewers for their contribution to the peer review of this work.

Reprints and permissions information is available at www.nature.com/reprints.